A lubrication model with slope-dependent disjoining pressure for modeling wettability alteration

Mojtaba Norouzisadeh, Philippe Leroy, Cyprien Soulaine

Computer Physics Communications 298 (2024) 109114

Contents lists available at ScienceDirect

Computer Physics Communications

journal homepage: www.elsevier.com/locate/cpc

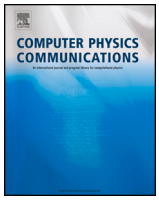

Computational Physics

A lubrication model with slope-dependent disjoining pressure for modeling wettability alteration ☆

Mojtaba Norouzisadeh [a,*], Philippe Leroy [b], Cyprien Soulaine [a]

[a] Institut des Sciences de la Terre d'Orléans, Université Orléans, CNRS, BRGM, 1A rue de la Férollerie, 45071 Orléans, France
[b] BRGM, French Geological Survey, 45100 Orléans, France

ARTICLE INFO

Dataset link: https://github.com/moji-n/Lubrication_for_thinfilm

Keywords:
Wettability alteration
Disjoining pressure
Lubrication model
Thin-film instability

ABSTRACT

We present the algorithm and the source code of our numerical model to characterize the wettability of a three-phase system. Wettability is imperative in describing two-phase flow in subsurface geo-environmental applications, including storage of carbon dioxide in deep saline aquifers and groundwater remediation. Although the concept of contact angle is widely used to characterize the affinity of a fluid pair with a solid substrate, it does not accurately describe wettability alteration due to changes in pH and salinity. The latter arises from inter-molecular interactions, which are dominant in the three-phase contact region where the solid, wetting, and non-wetting fluids meet each other. We developed a physically-rooted lubrication model for thin films to model wettability alteration and replace the concept of contact angle. The model accounts for inter-molecular forces, including van der Waals, electric double layer, and hydration potential through a disjoining pressure. Unlike other approaches, we introduce a slope-dependent disjoining pressure. We present the implementation algorithm and the source code. The model has been thoroughly verified and used to investigate the role of salinity and pH on wettability. We find out that the slope-dependent disjoining pressure and the precursor film thickness alter the stability of the spreading.

1. Introduction

Multi-phase flow occurs in underground reservoirs such as petroleum reservoirs or aquifers. Understanding the flow inside these reservoirs helps us to maintain and develop the reservoirs more efficiently. One of the key parameters in studying multi-phase flows is wettability, which describes the interaction of the different flowing phases with the solid substrate [32,46,61]. However, determining the system wettability is not a straightforward task as it varies with the different conditions of the system including interface velocity [44], pressure [43], salinity [29,28] and ion type [8], pH [47], temperature [49] and droplet size [14]. In addition, some studies suggest that wettability alteration takes place in the reservoir during exploitation; *e.g.* low-salinity water injection for enhanced oil recovery [1,41], carbon capture and storage (CCS) in saline aquifers [45,59,10], and groundwater remediation [34].

Current approaches to measure wettability through the contact angle are limited because they can not account for the variations in pH, salinity, temperature, and pressure unless the measurement is done for each specific condition. At the *three-phase contact point* (TPCP), where the solid substrate and two immiscible fluid phases meet each other, inter-molecular forces become as important as larger scale effects including viscous, surface tension, and gravity forces [7]. These inter-molecular forces are not considered properly when using the "macroscopic" (continuum-scale) contact angle concept. Moreover, a precursor liquid film pre-wetting the solid surface after the TPCP has been observed experimentally [52,23], which is not considered in the contact angle concept. The precursor film thickness can grow from approximately 1 nm up to 1 μm [51,23]. In this range of thickness, the effect of inter-molecular forces on the film becomes significant. These molecular interactions are described with the help of disjoining pressure, Π, that varies with the thickness of the film, h [17]. The disjoining pressure is due to the overall inter-molecular interaction of the two interfaces (*i.e.*, solid/fluid and fluid/fluid interfaces) of the thin film comprising of dispersion, electrostatic, and structural components [7]. The disper-

☆ The review of this paper was arranged by Prof. Peter Vincent.

* Corresponding author.
E-mail address: mojtaba.norouzisadeh@cnrs-orleans.fr (M. Norouzisadeh).

https://doi.org/10.1016/j.cpc.2024.109114
Received 29 August 2023; Received in revised form 23 December 2023; Accepted 26 January 2024
Available online 1 February 2024

Nomenclature

Constants

e	elementary charge	$1.602\,176\,634 \times 10^{-19}$ C
ϵ_0	vacuum permittivity	$8.854\,187\,812\,8 \times 10^{-12}$ F m^{-1}
k_B	Boltzmann factor	$1.380\,649 \times 10^{-23}$ J K^{-1}
g	gravity	9.81 m s^{-2}

Electric double layer

ψ, Ψ	electrostatic potential, dimensionless form	V
ζ	zeta potential	V
κ	Debye length	m^{-1}
ρ_∞	ionic strength	mol L^{-1}
ϵ	relative permittivity	

Lubrication model

u	velocity	m s^{-1}
p	pressure	kg m^{-1} s^{-2}
v_s	depth-averaged velocity	m s^{-1}
ρ_i	density of phase i	kg m^{-3}
q_s	2-D film flow rate	m^2 s^{-1}
μ	viscosity	kg m^{-1} s^{-1}
λ	slip length	m
M	fluid mobility	m^3 Pa^{-1} s^{-1}
$\mathbb{M}$	bi-Laplacian pseudo mobility	m^4 s^{-1}
$\mathcal{M}$	Laplacian pseudo mobility	m^2 s^{-1}
$\mathbb{T}$	interface shear contribution in the lubrication model	m^2 s^{-1}
Ca	capillary number	
B_o	Bond number	

Other symbols

$\mathbb{P}$	energy potential	kg m^{-1} s^2
θ	contact angle	
σ	interfacial tension	J m^{-2}
T	temperature	K
h	film thickness	m
h_x, h_{xx}	slope and curvature of the film	
$\mathbb{W}, W$	free energy, inter-molecular energy	J m^{-2}
Π	disjoining pressure	kg m^{-1} s^2
A	Hamaker constant	J

sion force is usually referred to as *Van der Waals* (VDW) force since it makes up most of VDW force when at least one of the constituents of the interaction is non-polar [27]. The dispersion forces arise from the fluctuation of the electromagnetic field in proximity to the interface [15]. The electrostatic component of the disjoining pressure, also called the electric double layer (EDL) component, is due to the presence of ions locally in excess or deficiency in the film while having charged interfaces [15]. The structural component of the disjoining pressure, also known as non-DLVO force, is due to the orientation and ordering of the molecules at the interfaces and several layers of molecules away.

The knowledge of inter-molecular interactions can lead to assessments of the static (or equilibrium) contact angle. Taheriotaghsara et al. [48] studied the alteration in wettability of a brine-calcite-oil system when changing the salinity of the brine. They observed the change in contact angle due to a change in disjoining pressure curves. For a similar case, [36] used Navier-Stokes equations in combination with the disjoining pressure quantity to obtain the time-scale of the transport of ions from the bulk to the contact region. This time scale corresponds to the time it can take for a change in wettability by changing the bulk salinity. In an experiment, Schwartz et al. [39] measured the contact line force in a capillary tube with multiple air bubbles inside, and they showed that the solid surface roughness is not the sole cause for contact angle hysteresis. Kuchin and Starov [30] developed a theory to model the effect of advancing and receding hysteresis by introducing in their model disjoining pressure curves with two local minima while not resolving any hydrodynamic equations.

Hydrodynamic of thin films can be resolved using diffuse-interface models [40], interface formation models [42], and *lubrication approximation* models [37,35,12]. The latter can be combined with disjoining pressures to include inter-molecular interactions on the thin film [51]. Huh and Scriven [26] showed that assuming a pre-deposited film on the solid is necessary to uphold the lubrication assumption. Teletzke et al. [51] categorized the films into thin-thin film (a few molecules diameter thickness) where the dynamic is mainly diffusive, thick-thin film (up to a few micrometers) where the effect of disjoining pressure is included in a lubrication model and thick film (bigger than a few micrometers) where the effect of disjoining pressure is negligible. They also showed that the hysteresis of the contact angle, *i.e.*, the difference in values of advancing and receding contact angle, does not only depend on the surface roughness but also results from an equilibrium-seeking behavior of the film. This behavior was studied in the context of film stability and rupture [35,6,3] through the linear stability analysis.

A common practice to track the spreading of a droplet using lubrication models is to use disjoining pressures for "flat" thin films [60,2]. For example, Wray et al. [57] studied the deposition of coffee rings using disjoining pressure. They found that applying an external electric field enhances or diminishes the ring formation. Barrett and Ajaev [4] developed a model for considering the evaporation of sessile drops spreading in which they highlight a relationship between disjoining pressure and evaporation rate by changing the contribution of the electrostatic component of the disjoining pressure. A comprehensive review of evaporation for sessile drops can be found in Wilson and D'Ambrosio [56]. In such cases, the disjoining pressure only depends on the film thickness, $\Pi(h)$. The observation of non-zero contact angles at the nanometric scale, however, contradicts this assumption [9]. This situation is particularly true for partially wet systems.

To overcome this limitation, researchers have derived disjoining pressure curves for wedge structures mimicking the angle formed by the fluid-fluid interface and the solid substrate [58,13,20] and for general curved interfaces [55]. It results in disjoining pressures that depend on higher-order derivatives of the film thickness, $\Pi(h, h_x, h_{xx})$. Alizadeh Pahlavan [3] studied the effect of disjoining pressure with higher derivatives on droplet spreading. Their approach leads to a non-zero contact angle at TPCP. However, they used a Lennard-Jones potential type for the disjoining pressure to account for repulsive forces, including EDL and structural force. The use of appropriate models for the said repulsive forces, in addition to the slop-dependent dispersion component, is important since it can influence film stability. It can also provide the necessary tools to study the effect of fluid properties such as salinity and pH on the evolution of film.

In this paper, we investigate the mechanisms occurring in the three-phase contact region, where inter-molecular interactions play a significant role. For that, we propose a comprehensive lubrication model for thin films that includes inter-molecular interactions through the concept of disjoining pressure. In the derivation, we included the dependency of inter-molecular force on the slope of the film to accurately model the non-zero slope of the film at the TPCP. This model can assess the wettability behavior of a three-phase system and its dependency on parameters such as salinity and pH.

The paper is organized as follows. In Section 2, we introduce the mathematical model that we developed to investigate moving contact

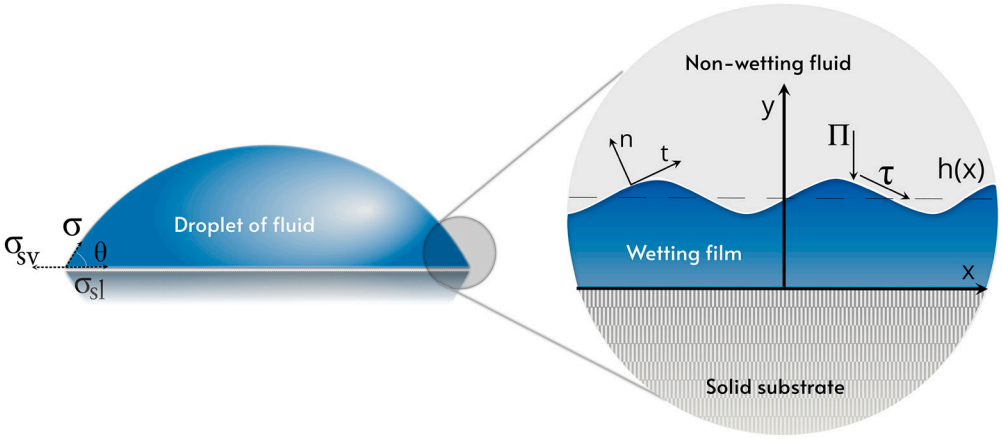

Fig. 1. 2D sketch of the thin wetting film sandwiched in between the solid substrate and the non-wetting fluid. Both inter-molecular interactions and fluid flow exert an excess stress – with a normal (Π) and a tangential (τ) component – on the fluid-fluid interface. The inter-molecular interaction in the film can be expressed as a normal stress on the boundary of the film.

lines. In Section 3, we detail our numerical strategy to solve the lubrication model for thin film. In Section 4, we present simulations of the spreading of droplets. We start with two validation cases to verify the robustness of the numerical implementation. Then, we use the lubrication model combined with disjoining pressure model to investigate wettability alteration due to a change in pH and salinity. Finally, we close our manuscript with a summary and perspectives.

2. Mathematical model

In this section, we introduce our mathematical model to simulate the spreading of droplets. It consists of a lubrication model for thin films (Section 2.2) that includes inter-molecular interactions described with the help of disjoining pressure concept (Section 2.3) and discretized using the finite difference method (Section 3).

2.1. Free energy for thin film

Let's consider a two-dimensional (2D) film of thickness, $h(x)$, varying along the x direction as illustrated in Fig. 1. As the film is not a flat surface, we define the slope as the space derivative, $h_x = \frac{\partial h}{\partial x}$. The free energy of the film, $\mathbb{W}$ (J m^{-2}), includes the surface tension and gravity effects as well as the inter-molecular interaction effects,

$$\mathbb{W}\left(h, h_x\right) = \sigma\sqrt{1+h_x^2} + \sigma_{SL} - \sigma_{SV} + \frac{1}{2}\rho g h^2 + W(h, h_x), \tag{1}$$

where $\sigma\sqrt{1+h_x^2}$ is the surface tension energy of two fluid phases, σ_{SL} and σ_{SV} are the surface energies of solid with the two fluid phases, $\frac{1}{2}\rho g h^2$ is the gravitational energy, and W is the inter-molecular energy that is described in detail in the next section. Surface and gravitational energies represent macroscopic effects, while inter-molecular energy describes microscopic interactions. Note that in the long-wave approximation, the slope of the fluid-fluid interface is small ($h_x \ll 1$), and using Taylor series $\sqrt{1+h_x^2} \approx 1 + \frac{h_x^2}{2}$.

In practice, we define the energy potential, $\mathbb{P}\left(h, h_x, h_{xx}\right)$, obtained using the variational derivative of the free energy with respect to height,

$$\mathbb{P}\left(h, h_x, h_{xx}\right) = \frac{\delta \mathbb{W}}{\delta h} = \left(\frac{\partial \mathbb{W}}{\partial h} - \frac{\partial}{\partial x}\left(\frac{\partial \mathbb{W}}{\partial h_x}\right)\right). \tag{2}$$

As the disjoining pressure, Π, is minus the variational derivative of the inter-molecular free energy, $\Pi\left(h, h_x, h_{xx}\right) = -\frac{\delta W}{\delta h}$, (see more details in Section 2.3) then the film potential,

$$\mathbb{P}\left(h, h_x, h_{xx}\right) = -\sigma\frac{\partial^2 h}{\partial x^2} + \rho g h - \Pi\left(h, h_x, h_{xx}\right), \tag{3}$$

depends on the surface tension force where $h_{xx} = \frac{\partial^2 h}{\partial x^2}$ is the interface curvature, on the gravity potential, and on the inter-molecular forces.

2.2. Lubrication model for thin films

Our model relies on the lubrication approximation to simulate the spreading of a droplet. Lubrication approximation is a reduced-order model of Navier-Stokes equations in which one dimension – the film thickness – is smaller than the other two (see Fig. 1). The evolution equation for the film thickness, h, is obtained by integrating the Navier-Stokes equations over the film thickness [37]. In this paper, we consider a two-dimensional system that reduces into a one-dimensional (1D) evolution equation. Extrapolation to three-dimensional systems follows similar developments. The integration of the mass balance equation reads,

$$\frac{\partial h}{\partial t} + \frac{\partial q_s}{\partial x} = 0, \tag{4}$$

where $h(x)$ is the film thickness (in m), $q_s = h v_s$ is flow rate within the film (in m^2/s), and v_s is the depth-averaged film velocity (in m/s). The latter is obtained by integrating the Stokes momentum equation between two parallel interfaces and using the long-wave approximation (*i.e.*, the wavy aspect of the fluid-fluid interface is negligible with respect to the size of the system). The driving force magnitude is a pressure-like gradient, $\partial\mathbb{P}/\partial x$, that accounts for gravity, interface curvature, and inter-molecular forces, as we will see later on. The final form of v_s strongly depends on the fluid-solid (*e.g.*, no-slip or partial slip, λ) and fluid-fluid boundary conditions (*e.g.*, free surface or mutual shear-stress, τ). A generic form of the resulting mass flow rate reads,

$$q_s = -M(h)\frac{\partial \mathbb{P}}{\partial x} + \mathbb{T}(h), \tag{5}$$

where $M(h)$ is the fluid mobility (in $\frac{\text{m}^3}{\text{Pa.s}}$), $\mathbb{T}(h)$ (in m^2/s) accounts for mutual shear stress at the fluid-fluid interface, and for space variations of the surface tension, and $\mathbb{P}$ is the pressure (in Pa) within the film. Expressions of $M(h)$ and $\mathbb{T}(h)$ are provided in Table 1 for various fluid-fluid and fluid-solid conditions. The mobility term, M, depends on the fluid-solid boundaries. The standard formula, $M(h) = \frac{h^3}{3\mu}$, corresponds to cases in which the wetting fluid has a no-slip behavior at the solid surface. Such a mobility expression, however, tends towards zero if the film thickness is zero, leading to an ill-posed equation, and requires to account for a precursor film – artificial or real – that always wets the solid surface [19]. A Navier slip describing the fluid-solid boundary condition can circumvent this issue where $u|_{y=0} = \lambda \left.\frac{\partial u}{\partial y}\right|_{y=0}$. The mobility is, then, modified to account for the Navier slip length, λ. When

Table 1
Mobility for fluid-solid interface and the stress boundary condition for fluid-fluid interface term in the lubrication model.

	Mobility, $M(h)$	$\mathbb{T}(h)$
No slip	$\frac{h^3}{3\mu}$	$\frac{h^2}{2\mu}\left(\frac{\partial\sigma}{\partial x}+\tau\right)$
Navier slip	$\frac{1}{\mu}\left(\frac{h^3}{3}+\lambda h^2\right)$	$\frac{1}{\mu}\left(\frac{h^2}{2}+\lambda h\right)\left(\frac{\partial\sigma}{\partial x}+\tau\right)$

considering free surfaces, *e.g.*, a droplet of oil surrounded by air, the hydrodynamic of the fluids is decoupled, and the shear stress in $T(h)$ is $\tau = 0$. Note that this hypothesis is no longer true for fluid pairs of moderate viscosity ratio [38]. In this case, it is necessary to couple the lubrication model with a Navier-Stokes based solver that computes the hydrodynamics within the non-wetting phase, and, therefore, the mutual shear-stress, τ [2].

Finally, combining the mass balance (Eq. (4)) with the mass flow rate in the film (Eq. (5)) and the energy potential equation (Eq. (3)), the evolution equation of the film thickness reads [35,3,33]:

$$\frac{\partial h}{\partial t} = \frac{\partial}{\partial x}\left(M(h)\frac{\partial}{\partial x}\left(-\sigma\frac{\partial^2 h}{\partial x^2}+\rho g h-\Pi\left(h,h_x\right)\right)-\mathbb{T}(h)\right). \tag{6}$$

This is the equation that is solved numerically in this paper (see Section 3). The challenge is two-fold: first, the bi-Laplacian operator associated with the interface curvature is a fourth-order space derivative that necessitates dedicated treatment, and second, the equation is non-linear.

2.3. Inter-molecular interactions and disjoining pressure

In thin films and at the vicinity of the three-phase contact region, the thickness of the wetting fluid becomes comparable with the range of inter-molecular interactions described through the concept of disjoining pressure (Π). The latter is evaluated through the knowledge of the dispersion (Van der Waals, Π_{VDW}), electrostatic (Electric Double Layer, Π_{EDL}), and structural (Π_{str}) components [16]:

$$\Pi = \Pi_{VDW} + \Pi_{EDL} + \Pi_{str}. \tag{7}$$

The combination of Van der Waals and Electric Double Layer interactions is also known as the DLVO interaction (short for Derjaguin, Landau, Verwey and Overbeek [18,53]). The structural or steric component of the disjoining pressure is related to the structure and the molecules' orientation close to the interface. All types of interactions mentioned previously are long-range interactions, *i.e.* their amplitude varies with the film thickness, h. Because films are not always parallel to the solid substrate, we will see that the inter-molecular forces can be slope-dependent (*i.e.*, they vary with h_x as well). In practice, we use the inter-molecular free energy, W, instead of the disjoining pressure to provide a more general equation. We have,

$$W = W_{VDW} + W_{EDL} + W_{str}. \tag{8}$$

The disjoining pressure is obtained from energy (W) using the variational derivative,

$$\Pi(h,h_x) = -\frac{\delta W}{\delta h} = -\left(\frac{\partial W}{\partial h}-\frac{\partial}{\partial x}\left(\frac{\partial W}{\partial h_x}\right)\right). \tag{9}$$

In the following, we introduce the different components used in this article to model the spreading of a droplet.

2.3.1. Van der Waals

The dispersion component of the disjoining pressure is due to the polarization of atoms and molecules and exists for even non-polar molecules. It is described by the Van der Waals (VDW) energy. The VDW potential is often obtained for parallel interfaces and depends only on the film thickness. For non-uniform films with arbitrary surfaces, including wavy films, however, it also depends on higher derivatives of the film thickness, including slope and interface curvature [55]. The same is true for partially wet systems and small contact angles. Based on the work of Wu and Wong [58], Dai et al. [13] derived a VDW interaction energy that depends not only on the film thickness but also on the slope of the interface. It reads,

$$W_{VDW} = -A_{123}\left(\frac{1}{12\pi h^2}+\frac{h_x^2}{16\pi h^2}\right), \tag{10}$$

where $A_{123} = A_{22} - A_{12} - A_{23} + A_{13}$ is the Hamaker constant. The indices $1,2,3$ refer respectively to solid, wetting, and non-wetting fluid. Hamaker constant encompasses the polarizability and number density of the constituents. In the limit of thin films ($h_x \to 0$), Eq. (10) tends toward the classical form of Van der Waals energy, $W_{VDW} = \frac{-A_{123}}{12\pi h^2}$, that is derived formally for parallel interfaces of a thin film in contact with the vapor [27]. The corresponding disjoining pressure obtained with the variational derivative is, $\Pi_{VDW}(h,h_x) = -\frac{A_{123}(4-3h_x^2+3hh_{xx})}{24\pi h^3}$, that tends towards $\Pi_{VDW}(h) = \frac{-A_{123}}{6\pi h^3}$ for negligible slope.

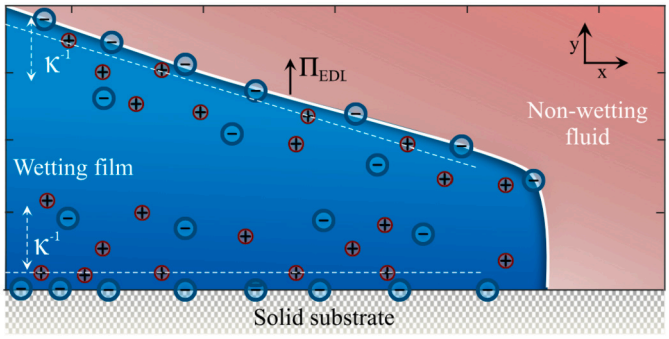

Fig. 2. The ions in the wetting film will get adsorbed on the interfaces with the solid and non-wetting fluid, and the counter-ions form a distribution in response to charges on the interface. The zeta-potential ζ is the electrostatic potential measured at a distance away from the interface (Stern layer thickness).

2.3.2. Electric double layer

The electrostatic component of the disjoining pressure is due to the interaction of ion species in the thin film with the fluid-solid and fluid-fluid interfaces. Ions are adsorbed on the interface surrounding the film (or repelled from it), which makes it electrostatically charged (Fig. 2). The counter-ions form a distribution in response to the charge of the interface. The distribution of counter-ions in the film, in addition to the interaction of the interfaces themselves with each other, creates an excess pressure that is called the electric double layer (EDL). Actually, there are two electric double layers – one for each interface bounding the wetting film – characterized by the electrostatic potential, ψ_i (in Volt), often assimilated to the zeta-potential, ζ_i that is defined as the electrostatic potential at the shear (or slipping) plane when wetting fluid flow occurs on the substrate. The range of interaction of EDL is characterized by the Debye-Hückel reciprocal length (in m^{-1}),

$$\kappa^2 = \frac{\rho_\infty e^2}{\epsilon\epsilon_0 k_B T}, \tag{11}$$

where ρ_∞ is the ionic strength in the bulk times the Avogadro number (in $\frac{\mathrm{mol}}{\mathrm{liter}}$), k_B is the Boltzmann constant (in $\frac{\mathrm{J}}{\mathrm{K}}$), T is temperature (in K), e is unit charge (in C), ϵ is relative permittivity of the fluid and ϵ_0 is the permittivity of vacuum (in $\frac{\mathrm{F}}{\mathrm{m}}$).

The EDL variation with respect to the film thickness is obtained by first specifying how the adsorbed charges on the interface are affected by the thin film thickness. For an oil-brine-calcite system, Taheriotaghsara et al. [48] by comparison of experimental measurements of contact angle and their results obtained with the disjoining pressure calcula-

tion, concluded that the assumption of constant charge on the oil-brine interface and constant electrostatic potential on the brine-calcite interface, as the thickness of the film of brine the changes provides the best match. Here, we consider constant charge in the film as the thickness of the film varies. Gregory [22] derived the EDL potential free energy for two parallel plates with constant charge in the film:

$$W_{EDL} = \frac{2\rho_\infty k_B T}{\kappa}\left[2\bar{\Psi}\ln\frac{B+\bar{\Psi}\coth\kappa h/2}{1+\bar{\Psi}} - \ln\left(\bar{\Psi}^2+\cosh\kappa h + B\sinh\kappa h\right)+\kappa h\right], \tag{12}$$

where $\Psi_i = \frac{e\psi_i}{k_B T}$ is the reduced electrostatic potential of the interface with solid ($i=1$) and with the non-wetting fluid ($i=2$), $\bar{\Psi} = \frac{\Psi_1+\Psi_2}{2}$ is the average potential, and $B = \sqrt{1+\bar{\Psi}^2\,\mathrm{csch}^2\,\kappa h/2}$. The corresponding disjoining pressure EDL component is

$$\Pi_{EDL}(h) = \rho_\infty k_B T\left[2B - \frac{(\Psi_1-\Psi_2)^2\exp(-\kappa h)}{B^2} - 2\right]. \tag{13}$$

Other EDL potentials can be derived by integrating the Poisson-Boltzmann equation with boundary conditions including constant charge, constant potential, and mixed-conditions [36]. The lubrication model for thin films that we introduce in this paper is generic, and all kinds of EDL potential can be used.

2.3.3. Structural component

In this article, the structural – or steric – component is considered a repulsive hydration force that decays monotonically with distance. We have,

$$W_{str}(h) = w_0 e^{-\frac{h}{\lambda_0}}, \tag{14}$$

where w_0 is the amplitude of the hydration in the order of $3-30\times 10^{-3}\mathrm{Jm}^{-2}$, and λ_0 is the decay length-scale in the order of $0.6-1.1$ nm [27]. Note that the hydration force changes with different types of cations solved in the water [27]. The corresponding disjoining pressure component is, $\Pi_{st}(h) = \frac{\omega_0}{\lambda_0}e^{-\frac{h}{\lambda_0}}$.

2.4. Film stability criteria

Films can be destabilized and rupture. A stability criterion for the lubrication equation, Eq. (6), is obtained using a linear stability analysis along the same lines as the work of Oron et al. [35]. It is achieved by applying a perturbation to a uniform solution, $h' = \exp(ikx+wt)$, where k is the wave number of the perturbation, and w is the perturbation frequency. By carrying out the derivative and setting the limit of the perturbation, $h'\to 0$, the condition for the decay of the perturbation and the film stability is:

$$k^2\left(\sigma+\frac{\partial\Pi}{\partial h_{xx}}\right)+\rho g+\frac{\partial\Pi}{\partial h}>0. \tag{15}$$

This criterion means that the stability depends on the wave number of the perturbation. If the disjoining pressure is only a function of h, meaning the contact angle is close to zero, we recover the film stability condition derived by Oron et al. [35]:

$$\rho g+\frac{\partial\Pi}{\partial h}>0. \tag{16}$$

A uniform deposited film can be the result of the adsorption of the wet phase on the solid surface before the spreading of the droplet and is dynamically stable. However, the rupture of the film discussed on this article is mainly due to the perturbation at the contact point when a droplet is placed on the film.

Based on this criterion and unless specified otherwise, the simulations of a spreading droplet will be set up with a precursor film that wet the solid substrate during the droplet spreading and whose thickness, b, is large enough to avoid thinning of the film leading to premature rupture. However, as the spreading continues, the thickness of the film might change at TPCP and fall in the unstable region.

3. Numerical implementation

The lubrication equation for thin films is solved in a one-dimensional horizontal solid surface to investigate the spreading of a droplet and the impact of wettability conditions. This is achieved by discretizing a non-dimensionalized lubrication equation with the Finite-Difference Method and solving it with an in-house MATLAB program.

3.1. Non-dimensionalization of the lubrication model for thin films

Expanding the disjoining pressure terms and using the chain rule, $\frac{\partial\Pi_{VDW}(h,h_x,h_{xx})}{\partial x} = \left(\frac{\partial\Pi_{VDW}}{\partial h}\right)\frac{\partial h}{\partial x}+\left(\frac{\partial\Pi_{VDW}}{\partial h_x}\right)\frac{\partial^2 h}{\partial x^2}+\left(\frac{\partial\Pi_{VDW}}{\partial h_{xx}}\right)\frac{\partial^3 h}{\partial x^3} = -\frac{A_{123}}{2\pi h^4}\left(1-\frac{3}{4}h_x^2-hh_{xx}\right)h_x + \frac{A_{123}}{8\pi h^2}h_{xxx}$, the lubrication equation (Eq. (6)) is recast into,

$$\frac{\partial h}{\partial t} = \frac{\partial}{\partial x}\left[\mathbb{M}(h)\frac{\partial^3 h}{\partial x^3}\right]+\frac{\partial}{\partial x}\left[\mathcal{M}(h)\frac{\partial h}{\partial x}\right]-\frac{\partial\mathbb{T}(h)}{\partial x}, \tag{17}$$

where the pseudo-mobility terms for the bi-Laplacian and Laplacian are,

$$\mathbb{M}(h) = -M(h)\left[\sigma-\frac{A_{123}}{8\pi h^2}\right],$$
$$\mathcal{M}(h) = M(h)\left[\rho g-\frac{A_{123}}{2\pi h^4}\left(1-\frac{3}{4}h_x^2+hh_{xx}\right)-\frac{\partial\Pi_{EDL}}{\partial h}-\frac{\partial\Pi_{st}}{\partial h}\right]. \tag{18}$$

The dimensionless evolution equation for the film thickness is obtained by introducing the scaling length and time, x_*, h_*, and t_*. We substitute $h=\tilde{h}h_*$, $x=\tilde{x}x_*$ and $t=\tilde{t}t_*$ into Eqs. (17)-(18) where $\sim$ denotes the non-dimensional variables. Using the characteristic time-scale $t_* = \frac{3\mu x_0^4}{\sigma h_0^3}$, we obtain,

$$\frac{\partial\tilde{h}}{\partial\tilde{t}} = \frac{\partial}{\partial\tilde{x}}\left[\widetilde{\mathbb{M}}(\tilde{h})\frac{\partial^3\tilde{h}}{\partial\tilde{x}^3}\right]+\frac{\partial}{\partial\tilde{x}}\left[\widetilde{\mathcal{M}}(\tilde{h})\frac{\partial\tilde{h}}{\partial\tilde{x}}\right]-C_T\frac{\partial\tilde{\mathbb{T}}(\tilde{h})}{\partial\tilde{x}}, \tag{19}$$

and the dimensionless pseudo-mobility terms are:

$$\widetilde{\mathbb{M}}(\tilde{h}) = -M(\tilde{h})\left[1-\frac{C_{VDW}\epsilon^2}{4\tilde{h}^2}\right]$$
$$\widetilde{\mathcal{M}}(\tilde{h}) = M(\tilde{h})\left[B_o-\frac{C_{VDW}}{\tilde{h}^4}\left(1-\frac{3}{4}\epsilon^2\tilde{h}_{\tilde{x}}^2+\epsilon^2\tilde{h}\tilde{h}_{\tilde{x}\tilde{x}}\right)-C_{EDL}\frac{\partial\widetilde{\Pi}_{EDL}}{\partial\tilde{h}}-C_{st}\frac{\partial\widetilde{\Pi}_{st}}{\partial\tilde{h}}\right], \tag{20}$$

where the Bond number is $B_o = \frac{\rho g x_0^2}{\sigma_0}$, the dimensionless coefficients for the disjoining pressure potentials are $C_{st} = \frac{\omega_0 x_0^2}{\lambda_0^2\sigma}$, $C_{EDL} = \frac{\rho_\infty k_B T\kappa x_0^2}{\sigma}$, and $C_{VDW} = \frac{A_{123}x_0^2}{2\pi h_0^4\sigma}$ and the coefficient for shear stress term corresponds to the viscosity ratio between the non-wetting and the wetting fluids, $C_T = \frac{\mu_{nw}}{\mu_w}$. The size aspect ratio is $\varepsilon = \frac{h_0}{x_0}$. The dimensionless mobility is found in Table 2.

3.2. Discretization

We obtain a system of linear equations using finite difference discretization for each point of the domain between two successive time-steps. The set of equations to be solved has the form:

Table 2
Dimensionless mobility and the stress boundary condition term in the lubrication model.

Fluid-solid boundary	$M(\tilde{h})$	$\mathbb{T}(\tilde{h})$
No-slip	$\tilde{h}^3$	$\frac{\tilde{h}^2}{2}\left(\tilde{\sigma}_{\tilde{x}}+\tau\right)$
Navier slip	$\tilde{h}^3+3\tilde{\lambda}\tilde{h}^2$	$\left(\frac{\tilde{h}^2}{2}+\tilde{\lambda}\tilde{h}\right)\left(\tilde{\sigma}_{\tilde{x}}+\tau\right)$

$$\frac{h_i^{t+1}-h_i^t}{\Delta t^t}+\theta\left(\sum_{n=-2}^{n=2}a_n h_{i+n}\right)^{t+1}+(1-\theta)\left(\sum_{n=-2}^{n=2}a_n h_{i+n}\right)^{t}=0. \tag{21}$$

This discretization is second-order in space (central difference) and second-order in time because we use the Crank–Nicolson method with $\theta=\frac{1}{2}$. The evolution equation for the film thickness comprised a second-order differentiation for the gravity and height-dependent inter-molecular potential and a fourth-order differentiation for the curvature and slope-dependent inter-molecular potential. The discretization of the fourth-order differential term in Eq. (17) for a uniform mesh spacing is:

$$\begin{aligned}\frac{\partial}{\partial x}\left[\mathbb{M}(h)\frac{\partial^3 h}{\partial x^3}\right]&=\mathbb{M}_{i+1/2}\frac{h_{i+2}-3h_{i+1}+3h_{i+1}-h_{i+1}}{(\Delta x)^4}\\&\quad-\mathbb{M}_{i-1/2}\frac{h_{i+1}-3h_i+3h_{i-1}-h_{i-2}}{(\Delta x)^4},\end{aligned} \tag{22}$$

and discretization of the second-order differential term in Eq. (17) using finite-difference method (FDM) with a central difference is:

$$\frac{\partial}{\partial x}\left[\mathcal{M}(h)\frac{\partial h}{\partial x}\right]=\mathcal{M}_{i+1/2}\frac{h_{i+1}-h_i}{(\Delta x)^2}-\mathcal{M}_{i-1/2}\frac{h_i-h_{i-1}}{(\Delta x)^2}, \tag{23}$$

Here, we only mention the expressions for the uniform spacing one-dimension mesh. However, the equation can be rewritten for any arbitrary spacing. This is what we have done to implement Adaptative Mesh Refinement techniques.

To ensure the positivity of the solution for all film thicknesses and the convergence of the scheme, we used the modification introduced in Zhornitskaya and Bertozzi [62], Diez et al. [19] as the regularization of the mobility term. The regularization comprised of imposing a precursor film on the domain $h(x,0)\rightarrow h(x,0)+b$ and a modification for mobility term. This film is initially perceived as a numerical artifact to perform the simulation since a film thickness of zero will impose problems for the simulation by rendering the mobility term zero at the TPCP. However, when we are performing the simulation considering the inter-molecular forces, then the film thickness gains physical meaning, and the value is inferred by the disjoining pressure curve and its derivative. After lifting up the initial solution, the mobility term for the fourth-order differentiation undergoes a regularization [19]:

$$\mathbb{M}^*(h)=\frac{\mathbb{M}(h)h^4}{b^a\mathbb{M}(h)+h^4}. \tag{24}$$

Interpolation of the mobility term on the cell faces for the fourth-order differentiation is done as:

$$\mathbb{M}_{i+1/2}=\begin{cases}\frac{h_{i+1}-hi}{g_{i+1}-g_i} & h_{i+1}\neq h_i\\ \mathbb{M}(h_i) & h_{i+1}=h_i\end{cases}\quad\text{and}\quad g=\int\frac{dh}{\mathbb{M}(h)}, \tag{25}$$

meanwhile, the interpolation of mobility for the second-order differential terms is the arithmetic mean:

$$\mathcal{M}_{i+1/2}=\frac{\mathcal{M}(h_i)+\mathcal{M}(h_{i+1})}{2}. \tag{26}$$

3.3. Mesh and adaptive mesh refinement

In order to obtain accurate results, the mesh size in the vicinity of TPCP should be in the same order of magnitude as the precursor film thickness. This is because the film thickness used in the mobility term becomes small and comparable with the precursor film. Therefore, we used a non-uniform mesh, which is coarse in most parts of the domain and gets finer close to the TPCP. As the TPCP location changes with the film spreading, we implemented an adaptative mesh refinement (AMR) scheme to follow the movement of TPCP and dynamically refine the mesh close to the contact point. When the mesh is modified, new nodes are created with unknown values for the thickness. We use linear interpolation to find the value for the film thickness on these points.

3.4. Solution algorithm

The simulation starts with creating a mesh over the initial droplet profile. We set a symmetric condition for the center of the droplet, and we specify $\frac{\partial h}{\partial x}=0$ and $\frac{\partial^3 h}{\partial x^3}=0$ at the other end of the 1D domain to describe an infinite boundary. Then, the coefficient matrix of the linear system is populated using the mobility values.

The calculation of the inter-molecular terms in the mobility terms in Eq. (17) is done explicitly since they contain nonlinear terms. Therefore, we imposed a loop for each time step to make sure the error caused by this implementation is smaller than a set criterion (10^{-8}). If the criteria can't be reached within a finite number of iterations, the time-stepping is reduced. In order to speed up the simulation, the time interval increases as the simulation progress, and it is constrained by maintaining $max(error_i)<10^{-2}$ calculated by

$$error\approx\frac{2\Delta^t}{\Delta^{t-1}}\frac{\Delta^{t-1}h^{t+1}+\Delta^t h^{t-1}-(\Delta^{t-1}+\Delta^t)h^t}{(\Delta^{t-1}+\Delta^t)h^t}, \tag{27}$$

where Δ^i is the time-step at time i.

The flowchart of the algorithm written in MATLAB is illustrated in Fig. 3. It contains an inner loop for the convergence of the mobility interpolation terms and an outer loop for the advancement of time. The time-stepping is dynamic and is controlled by different criteria mentioned earlier. The simulation will stop if it reaches the designated end time or if the time-stepping becomes too small.

4. Results

In this section, we present and discuss the simulation of the spreading of a droplet using our lubrication model for thin film combined with disjoining pressure model. The two first cases (Sections 4.1 and 4.2) compare our model with reference solutions of an oil droplet surrounded by air spreading on a solid substrate to verify the robustness of the numerical implementation. Then, we investigate the effect of wettability alteration on the spreading of a film with different salinity and pH (Section 4.3), where we study the spreading of water on carbonate surface in presence of oil.

4.1. Evolution of films driven by curvature

The objective of this case is to verify the fourth-order derivative discretization with adaptive mesh refinement (AMR) in the lubrication equation and its numerical implementation. One-dimensional spreading of a droplet only driven by surface tension effects is compared with a self-similar analytical solution. This solution exists for a mobility term $M(h)=h$, and the curvature as the only driving force, [19], hence this solution is for the free energy density of the system

$$\mathbb{W}=\sigma\left(1+\frac{1}{2}h_x^2\right). \tag{28}$$

For a (dimensionless) droplet of height $h=1$ and radius $x=1$, centered on the coordinate $x=0$, and whose initial shape is given by,

$$h\left(x,t=0\right)=\begin{cases}\left[1-x^2\right]^2 & \text{if } |x|\leq 1,\\ 0 & \text{elsewhere,}\end{cases} \tag{29}$$

the self-similar evolution is

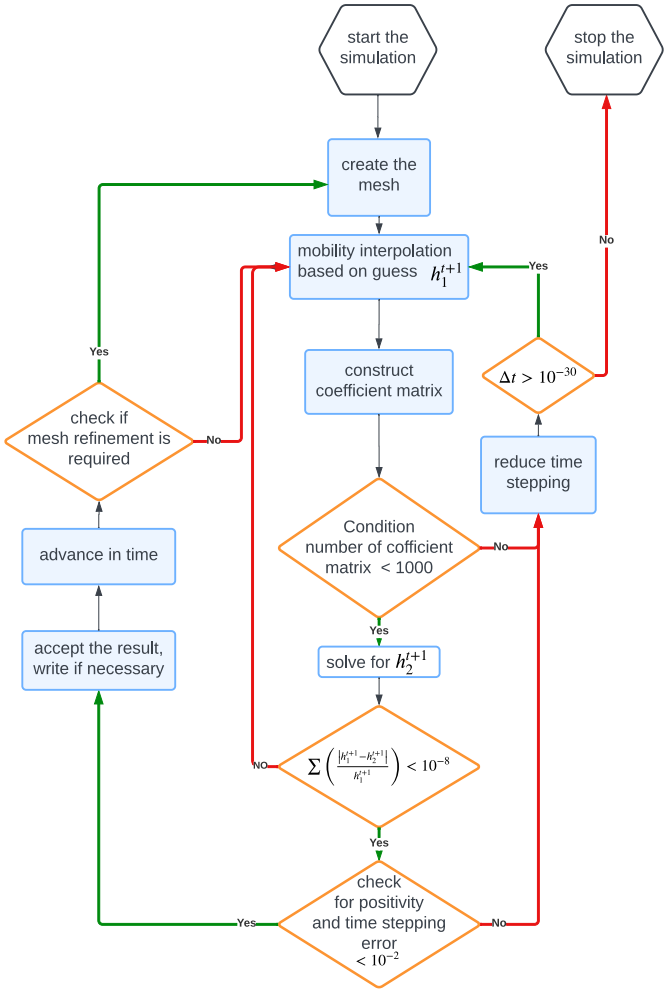

Fig. 3. The flowchart for the algorithm written in MATLAB to numerically solve the film thickness evolution equation.

$$h(x,t) = \begin{cases} (1+120t)^{-1/5}\left[1-\left(\frac{x}{x_f(t)}\right)^2\right]^2 & \text{if } |x| \le x_f(t), \\ 0 & \text{elsewhere,} \end{cases} \tag{30}$$

and $x_f(t) = (1+120t)^{1/5}$ is the radius of the droplet versus time.

The numerical model consists of a $x = 8$ cm long 1D domain. The droplet is deposited on top of a precursor film of thickness b to ensure positive values of the film thickness. The droplet boundaries are at $x = \pm 2$ cm and the initial condition for the film in the lubrication model is given by Eq. (29) by setting the dimensionless length and height as $x_* = 10h_* = 2$ cm. In all the numerical simulations, the time stepping is dynamic and ensures the criteria in Eq. (27), while the maximum dimensionless time-stepping is set to 10^{-6}.

In Fig. 4a, we compare the spreading of the droplet obtained using the lubrication simulation for $b = 0.001 \times h_*$ and AMR with the self-similar solution. The droplet spreads under the action of the surface tension. The droplet radius and the maximum height of the droplet are plotted in Fig. 4b. In Fig. 4c, we compare the mean square error (given by $\frac{1}{n}\sum_{i=1}^{n}\left(h_{analytical} - h_{simulation}\right)^2$) for a uniform mesh with spacing as small as b and the AMR mesh. The mean square error becomes smaller as b decreases. In addition, the error ceases to increase at later times (> 10 s) for small enough values of b (around $0.001 \times h_*$). The advantage of using AMR with respect to a uniform grid is the fewer grid points and faster simulation. For example, in the case where $b = 0.001 \times h_*$, a uniform grid has five times more points than the AMR. Meanwhile, the simulation took 22 times longer.

Table 3
Fluid properties used in Section 4.2 to simulate the spreading of a droplet driven by curvature and gravity.

phase	density kg m^{-3}	viscosity Pa s	surface tension N m^{-1}
silicon oil	968	0.2	0.021
air	1	1×10^{-6}	

The results are in very good agreement with the reference solution, which confirms the strength of the bi-Laplacian discretization with AMR.

4.2. Spreading of a droplet driven by curvature and gravity

The objective of this case is to verify the implementation of both gravity and curvature in the lubrication model. As there is no analytical solution for such a case [19], the verification is achieved by comparing the spreading of droplets obtained with the lubrication model and a Volume of Fluid approach. The latter is a Navier-Stokes-based interface capturing approach that is used as a reference solution to verify the relevance of the reduced-order lubrication model.

We consider a droplet of silicon oil surrounded by air. Fluid properties are summarized in Table 3. The initial shape of the droplet is a semi-ellipsoid described by $\left(\frac{x}{x_*}\right)^2 + \left(\frac{y}{h_*}\right)^2 = 1$ where $x_* = 2$ cm, $y_* = 0.2$ cm. The aspect ratio of the initial shape is consistent with the hypothesis of the lubrication model – *i.e.*, the film thickness is much smaller than the other dimension – which allows for a fair comparison between the two approaches. To focus on the effect of curvature and gravity avoiding challenges associated with the three-phase contact line, we consider a 20 μm ($0.01h_*$) thick silicon oil film at the surface of the solid substrate. At the time $t = 0$, the droplet spreads under the action of gravity and surface tension. Navier-Stokes simulation provides a two-dimensional mapping of the fluid evolution onto the computational domain. This mapping is then depth-averaged to form a reference film thickness profile that is compared with the solution of the lubrication model.

In the lubrication model, the free energy density is

$$\mathbb{W} = \sigma\left(1 + \frac{1}{2}h_x^2\right) + \frac{\rho g h^2}{2}, \tag{31}$$

and the mobility is $M(h) = \frac{h^3}{3\mu}$. The fluid-fluid interface is considered a free surface because the shear stress of air onto the oil droplet is negligible, and we have $\mathbb{T}(h) = 0$. The Bond number and the time scale used in the simulation are $B_o = 180$, and $t_0 = 1/580$. This corresponds to a one-dimensional domain of 4 cm and a gravity field, $g = 9.8$ m s^{-2}. The domain is discretized with non-uniform grid blocks, and AMR is used during the simulation at the tip of the droplet.

The Navier-Stokes reference solution is obtained using the Volume of Fluid solver of the Computational Fluid Dynamics open-source package OpenFOAM (https://www.openfoam.org), namely *interFoam* solver. The Volume of Fluid solves for the Navier-Stokes mass balance and momentum equations in both fluid phases as well as the evolution of the fluid distribution, α [24]. Surface tension effects due to interface curvature are described using Brackbill's force [5]. The computational domain consists in a two-dimensional 100 mm × 5 mm box meshed with a uniform grid whose spacing in x and y direction is $\Delta x = \Delta y = 0.02$ mm. The phase field, α, is initialized using the droplet shape used in the lubrication model with $x_* = 10y_* = 2$ cm, which corresponds to the same Bond number as in the lubrication simulation. A 0.02 mm thick film prewets the bottom boundary. The bottom edge is a no-slip condition. The top and right boundaries are set as zero-gradient for velocity, pressure, and phase field. The left side is set as symmetry. The simulation is run for 20 s with a constant time-step $\Delta t = 3 \times 10^{-7}$ s

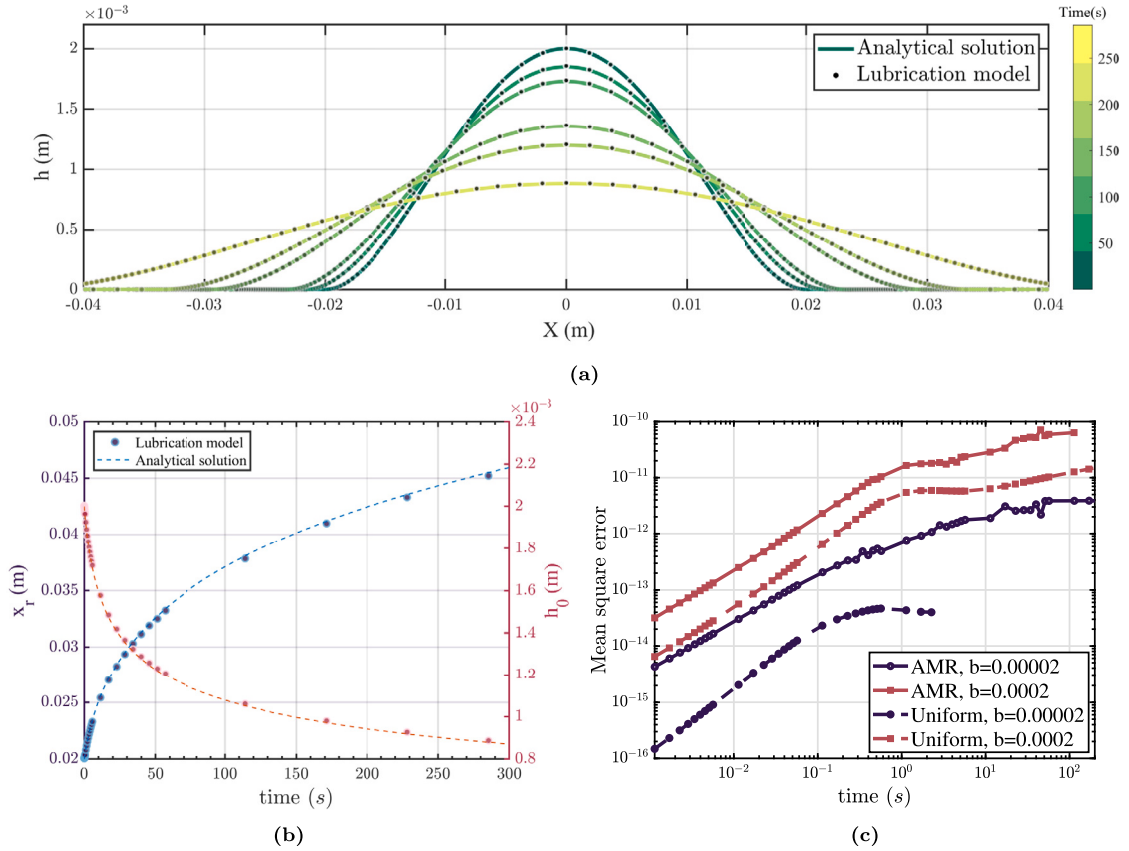

Fig. 4. Spreading of the droplet driven by the curvature, (a) lubrication model prediction versus analytical solution for the evolution of the droplet. The time is indicated by the color map on the right. The numerical results are in good agreement with the analytical solution. (b) The droplet radius and maximum thickness obtained from the lubrication model are compared with the analytical solution. (c) The mean square error of the lubrication model compared with the analytical solution for uniform and AMR mesh with different values of b.

that satisfies Brackbill's time-stepping criteria [5]. In order to obtain the film thickness along the horizontal direction from the Volume of Fluid simulation, the resulting two-dimensional phase field, α, is integrated over the vertical axis. The evolution of the droplet radius is obtained by integrating the phase field along the bottom boundary.

A comparison between the lubrication model and OpenFOAM Volume of Fluid results is seen in Fig. 5. We observe a very good agreement between the two approaches for the evolution of the droplet (Fig. 5a), the thickness of the droplet at the center, as well as the movement of the TPCP with respect to time (Fig. 5b). The overall difference between the lubrication model and the VOF approach predictions is very good and the mean square error is below 2.5×10^{-6}. These results give confidence in the robustness of the numerical implementation of the lubrication model. In the following, we investigate the spreading of a droplet with gravity, surface tension, and disjoining pressure.

We also investigated the effect of the droplet size on the spreading. Two oil droplets of $x_* = 2$ mm; $y_* = 0.2$ mm and $x_* = 10$ mm; $y_* = 1$ mm are considered. They correspond to Bond numbers of 1.8 and 180, respectively. At late time, the bigger droplet profile is close to a pancake shape, while the smaller droplet is closer to a lens shape. In Fig. 5c, the advancing contact angle is plotted against the capillary number for the velocity at the TPCP for times $> 10^{-1}$ s. We notice that both Ca-θ results fit Tanner's law (i.e., $\theta \propto Ca^{\sim 3}$ which suggests that the lubrication model captures the apparent contact angle due to hydrodynamic viscous bending.

4.3. Spreading of a droplet driven by curvature, gravity, and disjoining pressure

In this section, we investigate the spreading of water against oil on a calcite surface while changing the water's properties, including its salinity. This kind of simulation requires accounting for the effect of inter-molecular interactions in addition to surface tension and gravity potentials.

To model wettability alteration due to a change of salinity and pH, the free energy density of the film includes the curvature, gravity, and inter-molecular (Van der Waals, EDL, and hydration) interaction energy:

$$\mathbb{W} = \sigma\left(1 + \frac{1}{2}h_x^2\right) + \frac{\rho g h^2}{2} + \sigma_{SL} - \sigma_{SV} + W_{VDW} + W_{EDL} + W_{Str}. \quad (32)$$

We assume a no-slip boundary condition on the calcite surface, and the mobility term is $M(h) = \frac{h^3}{3\mu}$. We also neglect the effect of stress on the water-oil interface, $\mathbb{T}(h) = 0$.

4.3.1. Disjoining pressure for high- and low-salinity waters

We consider three different water solutions that differ by their salinity, namely a high-salinity water and two low-salinity waters with different pH in accordance with the work of Mahani et al. [31]. The high-salinity water is the formation water of a hydrocarbon reservoir, and the low-salinity water corresponds to diluted seawater by 25 times. Mahani's experiment was carried out to relate the wettability alteration in low-salinity water flooding to electrostatic measurements on the interfaces. Here, we used their measurements to evaluate the EDL potential

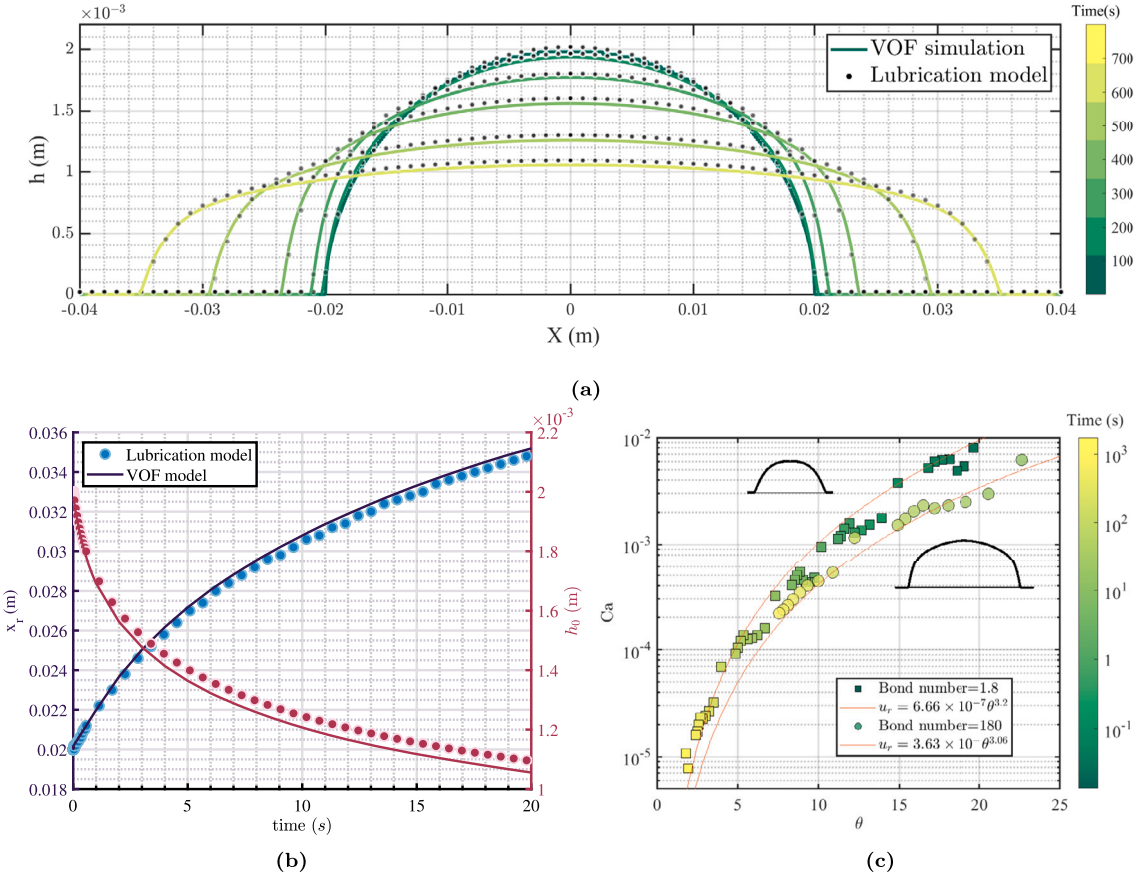

Fig. 5. Comparison of our lubrication model and a two-phase flow solver based on the Volume of Fluid (VOF) technique for the spreading of silicon oil against air on a flat surface including gravity and curvature forces. (a) Profiles of the spreading droplet at different times. The lubrication model shows good agreement with the VOF simulation. (b) Evolution of the wetted surface and of the droplet height using both the lubrication model and the VOF simulations. (c) Capillary number versus advancing contact angle for different Bond numbers. The fitted curves are based on Tanner's equation.

Table 4
Parameters used for simulation of spreading droplets considering curvature, gravity, and inter-molecular force.

VDW [25]					
Hamaker constant (A) J			1.3×10^{-20}		
EDL [31]					
water	ζ_1/ζ_2[mV]	ionic strength (ρ_∞)	pH	ϵ	T [K]
High-salinity	+5/-3	3.66	7		
Low-salinity (1)	-15/-25	0.035	7	78.54	300
Low-salinity (2)	+5/-20	0.035	12		
Hydration potential [27]					
Hydration amplitude (w_0) Jm^{-2}			30×10^{-3}		
Hydration length-scale (λ_0) nm			0.8		
Fluid properties					
water		density [kg/m^3]	viscosity [Pa×s]	surface tension [N/m]	
high-salinity		1000	10^{-3}	0.0118	
low-salinity		1000	10^{-3}	0.0131	

for the three water solutions. Inter-molecular interaction parameters are obtained using the values in Table 4. For both solutions, the Hamaker constant comes from Hough and White [25], and the hydration potential parameters come from Israelachvili [27]. For EDL calculation, the electric potential of the interface, ψ_i, is assumed to be equal to the zeta-potential of the interface, ζ_i.

The resulting disjoining pressures and their corresponding derivative versus thickness for the case of low- and high-salinity waters are plotted in Fig. 6. The first row (Fig. 6a, Fig. 6b) corresponds to a flat thin film whereas the second row (Fig. 6c, Fig. 6d) corresponds to a wedge with an angle of 45°. The film of low-salinity water (1) and (2) in the wedge case with an angle of 45° is stable for all the thicknesses since the

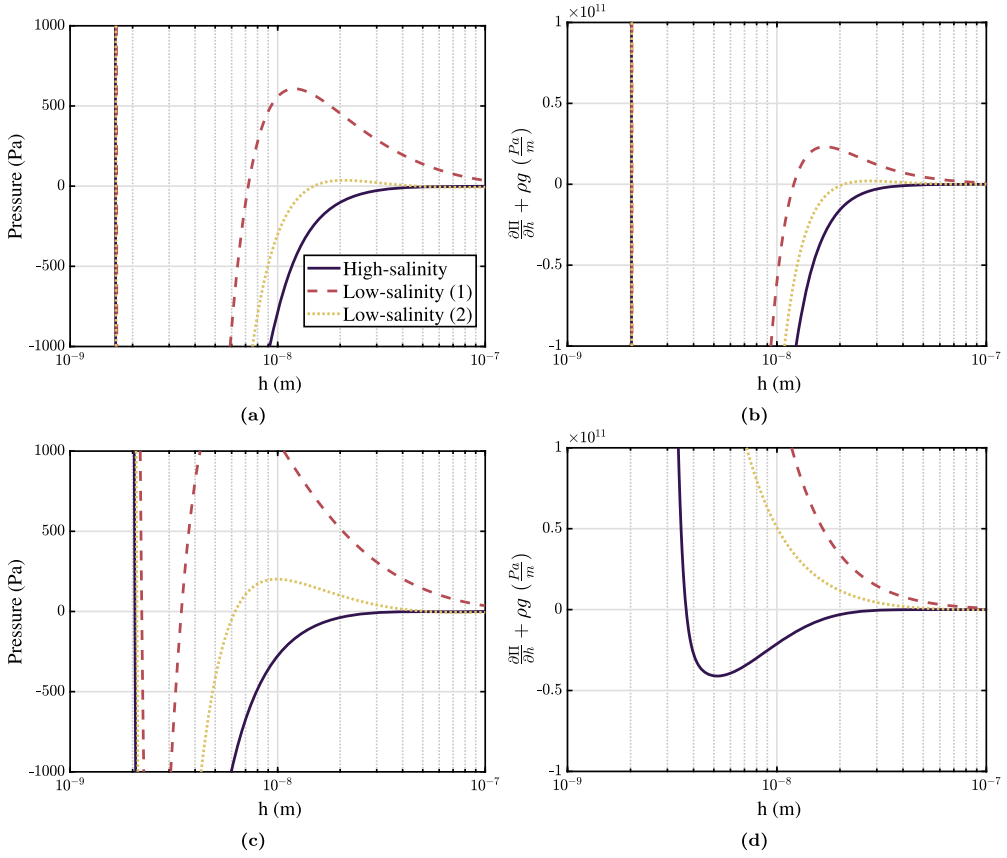

Fig. 6. Inter-molecular property for the thin film of water in the system of water/oil/carbonate. (a,b) Disjoining pressure and its derivative for a flat film. (c,d) Disjoining pressure and its derivative for a wedge film with the contact angle of 45 °.

derivative of disjoining pressure is positive, while for the high-salinity case, the stable thickness is below around 3 nm (Fig. 6d). However, by decreasing the angle, the range in which the film is stable changes. For the flat film, *i.e.*, zero angle, the derivative of the disjoining pressure is negative from very large thickness up until the thickness close to 2 nm for the high-salinity case. Whereas for the low-salinity (1) and (2), there is a mid-range thickness around 10 nm where the disjoining pressure and its derivative are positive, resulting in a thicker stable film compared to the high-salinity case. We consider the flat thin film curves for the stability analysis since it represents the lower value of film thickness for the film stability and the worst-case scenario.

4.3.2. *Impact of salinity and pH on wettability properties*

The initial shape of the droplet is a semi-ellipsoid described by $\left(\frac{x}{x_*}\right)^2+\left(\frac{y}{h_*}\right)^2=1$, where $x_*=0.1$ mm; $y_*=0.01$ mm corresponding to a Bond number of 0.0166. The computational domain is a 1D segment of length $4\times x_*$, discretized non-uniformly with $\Delta x_{max}=0.05\times y_*$ and $\Delta x_{min}=0.5\times b$. The droplet is deposited on a precursor film of thickness, $b=10$ nm, that is thick enough to avoid premature unstable films during spreading according to the stability criterion.

Simulations are run for 1 second or until the film ruptures. The evolution of the droplet spreading with the Bond number of 0.0166 is shown in Fig. 7a for the three different cases as well as the case without disjoining pressure. We also plot the evolution of the wetted area in Fig. 7b as well as the contact angle variation with respect to time (Fig. 7c). The latter is obtained by computing the slope of the interface at the inflection point. We observe different spreading patterns for the two types of water. On the one hand, the high-salinity water spreads for around 0.05 seconds until the precursor film gets ruptured, which stops the spreading. The equilibrium state corresponds to a contact angle $\theta\approx 6$. On the other hand, low-salinity (1) water droplet spreads faster, wetting the whole solid substrate, in agreement with the disjoining pressure curve (see Fig. 6a). The spreading of low-salinity water (2) follows a similar behavior to the high-salinity water, but the film rupture happens later. This situation corresponds to a contact angle, $\theta\approx 4$.

In Fig. 8, the advancing contact angle is plotted against the capillary number for the velocity of the TPCP during the spreading of the thin film for the time $> 10^{-3}$ s. The capillary number is defined as $Ca=\frac{\mu u}{\sigma}$. Interestingly, the intermediate-time data points fit into an equation of $Ca=a\times\theta^{\sim 3}$, similar to Tanner's law [50] or Cox-Voinov dynamic contact angle [54,11].

The different behaviors observed for the three waters are explained using the disjoining pressure derivative: a film with a thickness higher than ~ 10 nm is stable for low-salinity cases, whereas for the high-salinity water, films thicker than around 1 nm are unstable and will eventually rupture by introducing a perturbation. To analyze further the mechanisms leading to rupture, we plot the evolution of the minimum film thickness at the vicinity of the TPCP (see Fig. 9). We see an oscillatory behavior of the film thickness at TPCP versus time. This oscillation exists even in the absence of disjoining pressure (curvature is the only driving mechanism for the spreading), suggesting that instabilities are initiated by curvature effects. The oscillation can be enhanced or dampened based on the disjoining pressure. For the low-salinity water (1), the oscillation is dampened around a constant thickness corresponding to a stable film. Therefore, the TPCP spreads until complete wetting. For the low-salinity (2) and high-salinity waters, the minimum thickness decreases down to values for which the disjoining pressure corresponds to unstable films that eventually break up. For high-salinity water, the oscillations diverge, leading to a premature film rupture.

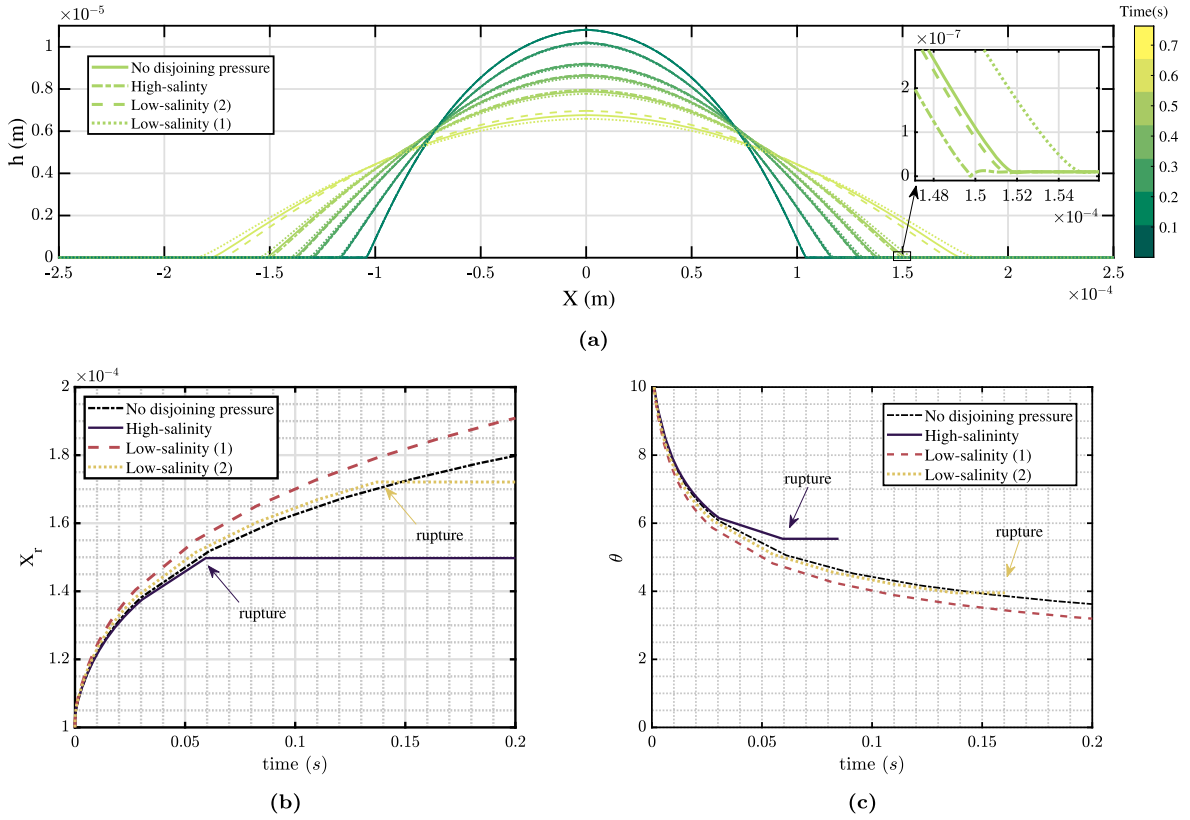

Fig. 7. Spreading of water in the system of water/oil/carbonate considering curvature, gravity, and disjoining pressure with the Bond number of 0.0166. (a) The plot of the water droplet profile for three different water types. Time is indicated by the color bar. In the inset plot, the profile of the film close to TPCP is shown at the time of rupture for high-salinity. The high-salinity water advances slower in comparison with the low-salinity cases and undergoes a rupture eventually. The transition of low-salinity (1) water to the precursor thickness occurs more smoothly compared to the high-salinity case. (b) Evolution of droplet radius. The spreading of high-salinity and low-salinity (2) water is halted at around 0.05 and 0.15 seconds, respectively, due to thinning of the precursor film at TPCP. (c) Variation of the contact angle at the inflection point with respect to time.

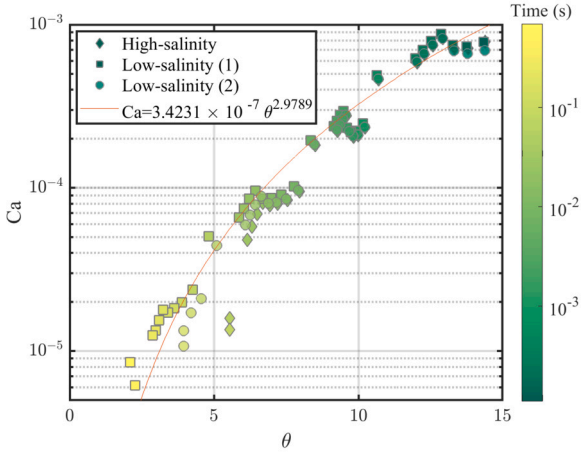

Fig. 8. Capillary number versus advancing contact angle for spreading of the thin film with different water salinity in the system of water/oil/carbonate considering curvature, gravity, and disjoining pressure. The fitted curves are based on Tanner's equation for contact angle.

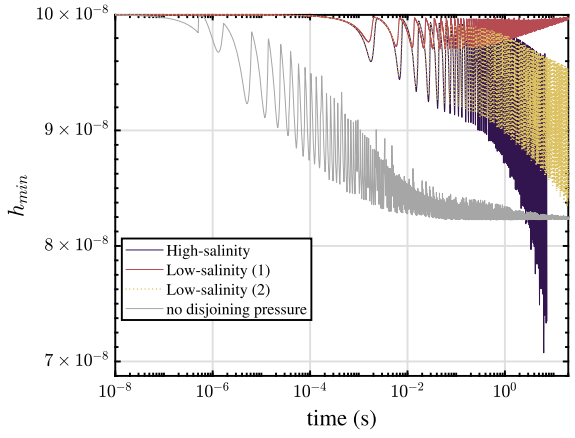

Fig. 9. The oscillation of TPCP thickness versus time for spreading of water with different properties. The oscillation in the case of low-salinity (1) gets dampened in late times, whereas for high-salinity, it grows until the rupture of the film. For low-salinity (2), the growth of amplitude of oscillation becomes steady in late times.

4.3.3. *Effect of the precursor film thickness*

In this part, we investigate the effect of the precursor film thickness on the droplet spreading for only the high-salinity water case because we are mainly interested in determining the effect of the initial precursor. We consider a precursor thickness b ranging from 0.5 to 80 nm. Different spreading behaviors are expected because the disjoining pressure derivative (see Fig. 6b) is negative for $b > 1$ nm (unstable film) and tends toward a positive asymptote for $0.2\ \text{nm} < b < 1$ nm.

The effect of the precursor film thickness on the droplet radius evolution and the time-to-rupture is seen in Fig. 10. We observe two spreading patterns leading to stationary droplets that depend on the

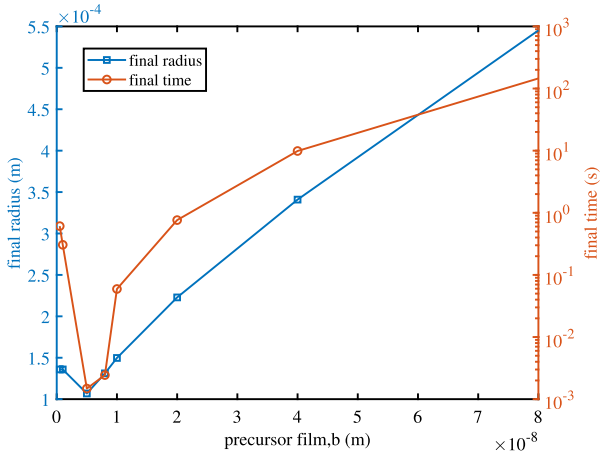

Fig. 10. The final radius of the droplet of high-salinity water spreading on the calcite surface in the presence of oil for different precursor water film thicknesses and its corresponding rupture time.

initial precursor film thickness, b: *i)* film rupture, and *ii)* TPCP equilibrium.

On the one hand, for precursor films larger than 1 nm, the droplet spreading comes to a halt after some time due to film rupture. This is expected as the disjoining pressure derivative is negative for $b > 1$ nm (see Fig. 6). The smaller the precursor films, the earlier the film rupture, and the smaller the droplet radius. Note that if the droplet radius evolves almost linearly with b, the time-to-rupture response is not linear.

On the other hand, for precursor films smaller than 1 nm, we observe an increase in the precursor film stability, for which the spreading stops not because of film rupture but because the TPCP slows down until it reaches an equilibrium state. This is expected because the disjoining pressure curve is strongly repulsive for $0.2 \text{ nm} < b < 1$ nm.

These simulations highlight two different behavior due to the initial precursor film. It means that for TPCP advancing on a dry surface, the film is stable, whereas, in advancing on a pre-wet solid, the film at TPCP will be unstable and causes rupture. Simulation results for the ultra-thin film should be interpreted cautiously because the continuum mechanics hypothesis breaks down for films below ~ 1 nm since the Knudsen number (ratio between mean free path over the length scale) at this thickness is around 0.1 corresponding to the transition between continuum scale and molecular scale [21].

5. Conclusion

We developed a lubrication model that accounts for inter-molecular interactions to model the wettability behavior of a three-phase system. The model is physically rooted and does not rely on the concept of contact angle. Instead, inter-molecular interactions are described using disjoining pressure concept, including Van der Waals, Electric Double Layer, and hydration interactions. This approach can predict wettability alteration due to the effect of fluid composition, salinity, and pH. Therefore, our lubrication model with slope-dependent disjoining pressure can be used to characterize contact angles for different chemical and physical parameters.

The numerical implementation of the model was verified using cases for which reference – analytical and numerical – solutions exist. The Adaptive Mesh Refinement feature is key to resolving the contact line dynamics in acceptable simulation times. A similar procedure can be used to extend our one-dimensional lubrication model to 2D.

The low- versus high-salinity water examples presented in this paper highlight the capabilities of our lubrication model for thin films to simulate wettability alteration due to a change in salinity conditions. Indeed, changing pH and salinity alters the EDL and, to some extent, the hydration force, which influences the precursor film stability and eventually leads to three spreading behaviors: spreading with complete wetting, droplet immobilization by film rupture, and immobilization without rupture by force equilibrium. We have also shown that the initial thickness of the precursor film strongly impacts the spreading of a droplet.

Future work will focus on the development of slope-dependent EDL models by solving the Poisson-Boltzmann equation with appropriate charge conditions at the fluid-fluid and fluid-solid interfaces. Our lubrication model for thin-film is an integrator for such inter-molecular considerations. Furthermore, the model can be modified to address spreading on the surface with roughness, as well as studying the chemical non-equilibrium system where the salinity/pH of the wetting phase changes as the film spreads. The dynamics of the non-wetting fluid has been neglected in this work. Future lines of research concern the coupling of our lubrication model with a Navier-Stokes-based solver to account for larger-scale hydrodynamics and the mutual shear stress at the fluid-fluid interface.

CRediT authorship contribution statement

Mojtaba Norouzisadeh: Conceptualization, Methodology, Software, Validation, Writing – original draft, Writing – review & editing, Formal analysis, Investigation. **Philippe Leroy:** Conceptualization, Formal analysis, Investigation, Supervision, Writing – review & editing. **Cyprien Soulaine:** Conceptualization, Formal analysis, Funding acquisition, Investigation, Methodology, Supervision, Validation, Writing – original draft, Writing – review & editing.

Declaration of competing interest

The authors declare the following financial interests/personal relationships which may be considered as potential competing interests:

Mojtaba Norouzisadeh reports financial support was provided by French National Research Agency.

Data availability

The model is implemented in MATLAB. The source-code presented in this article is available on the GitHub repository, https://github.com/moji-n/Lubrication_for_thinfilm. A brief description of the code is written in “README.md”.

Acknowledgements

The research leading to these results has received funding from the French Agency for Research (Agence Nationale de la Recherche, ANR) through the FraMatI project under contract ANR-19-CE05-0002 and the labex Voltaire ANR-10-LABX-100-01. The authors benefited from the use of the cluster at the Centre de Calcul Scientifique en région Centre-Val de Loire (CaSciMoDOT).

References

[1] Arastoo Abdi, Zahra Bahmani, Behnam Ranjbar, Masoud Riazi, Chapter 7 - smart water injection, in: Abdolhossein Hemmati-Sarapardeh, Mahin Schaffie, Mohammad Ranjbar, Mingzhe Dong, Zhaomin Li (Eds.), Chemical Methods, in: Enhanced Oil Recovery Series, Gulf Professional Publishing, ISBN 978-0-12-821931-7, 2022, pp. 313–356, https://www.sciencedirect.com/science/article/pii/B9780128219317000080.

[2] Moataz O. Abu-Al-Saud, Soheil Esmaeilzadeh, Amir Riaz, Hamdi A. Tchelepi, Pore-scale study of water salinity effect on thin-film stability for a moving oil droplet, J. Colloid Interface Sci. 569 (2020) 366–377.

[3] Amir Alizadeh Pahlavan, Moving contact lines, wetting transitions and interfacial instabilities in confined environments, PhD thesis Massachusetts Institute of Technology, 2018.

[4] James A. Barrett, Vladimir S. Ajaev, The effect of electrical double layers on evaporation of sessile droplets, J. Eng. Math. 134 (1) (2022) 10.

[5] Jeremiah U. Brackbill, Douglas B. Kothe, Charles Zemach, A continuum method for modeling surface tension, J. Comput. Phys. 100 (2) (1992) 335–354.

[6] J.P. Burelbach, S.G. Bankoff, S.H. Davis, Nonlinear stability of evaporating/condensing liquid films, J. Fluid Mech. 195 (1988) 463–494, https://doi.org/10.1017/S0022112088002484.

[7] Emmanouil Chatzigiannakis, Nick Jaensson, Jan Vermant, Thin liquid films: where hydrodynamics, capillarity, surface stresses and intermolecular forces meet, Curr. Opin. Colloid Interface Sci. (ISSN 1359-0294) 53 (2021) 101441, https://doi.org/10.1016/j.cocis.2021.101441, https://www.sciencedirect.com/science/article/pii/S135902942100025X.

[8] Cong Chen, Ning Zhang, Weizhong Li, Yongchen Song, Water contact angle dependence with hydroxyl functional groups on silica surfaces under co2 sequestration conditions, Environ. Sci. Technol. 49 (24) (2015) 14680–14687.

[9] Lei Chen, Jiapeng Yu, Hao Wang, Convex nanobending at a moving contact line: the missing mesoscopic link in dynamic wetting, ACS Nano 8 (11) (2014) 11493–11498, https://doi.org/10.1021/nn5046486.

[10] Pierre Chiquet, Daniel Broseta, Sylvain Thibeau, Wettability alteration of caprock minerals by carbon dioxide, Geofluids 7 (2) (2007) 112–122, https://doi.org/10.1111/j.1468-8123.2007.00168.x.

[11] R.G. Cox, The dynamics of the spreading of liquids on a solid surface. Part 1. Viscous flow, J. Fluid Mech. 168 (1986) 169–194.

[12] Richard V. Craster, Omar K. Matar, Dynamics and stability of thin liquid films, Rev. Mod. Phys. 81 (3) (2009) 1131.

[13] Bing Dai, L. Gary Leal, Antonio Redondo, Disjoining pressure for nonuniform thin films, Phys. Rev. E 78 (2008) 061602, https://doi.org/10.1103/PhysRevE.78.061602, https://link.aps.org/doi/10.1103/PhysRevE.78.061602.

[14] Yajun Deng, Lei Xu, Hailong Lu, Hao Wang, Yongmin Shi, Direct measurement of the contact angle of water droplet on quartz in a reservoir rock with atomic force microscopy, Chem. Eng. Sci. (ISSN 0009-2509) 177 (2018) 445–454, https://doi.org/10.1016/j.ces.2017.12.002, http://www.sciencedirect.com/science/article/pii/S000925091730739X.

[15] Boris Vladimirovich Derjaguin, Theory of Stability of Colloids and Thin Films, Springer, 1989.

[16] Boris Vladimirovich Derjaguin, NikolaĭVladimirovich Churaev, Vladimir Maksovich Muller, V.I. Kisin, Surface Forces, Springer, 1987.

[17] B.V. Derjaguin, N.V. Churaev, On the question of determining the concept of disjoining pressure and its role in the equilibrium and flow of thin films, J. Colloid Interface Sci. 66 (3) (1978) 389–398.

[18] B.V. Derjaguin, L. Landau, Theory of stability of highly charged lyophobic soils and adhesion of highly charged particles in solutions of electrolytes, Zh. Eksp. Teor. Fiz. 11 (1941) 801–818.

[19] Javier A. Diez, L. Kondic, Andrea Bertozzi, Global models for moving contact lines, Phys. Rev. E 63 (2000) 011208, https://doi.org/10.1103/PhysRevE.63.011208, https://link.aps.org/doi/10.1103/PhysRevE.63.011208.

[20] Aaron Dörr, Steffen Hardt, Electric-double-layer structure close to the three-phase contact line in an electrolyte wetting a solid substrate, Phys. Rev. E 86 (2) (2012) 022601.

[21] Mohamed Gad-el Hak, The fluid mechanics of microdevices—the freeman scholar lecture, 1999.

[22] John Gregory, Interaction of unequal double layers at constant charge, J. Colloid Interface Sci. 51 (1) (1975) 44–51.

[23] W. Bate Hardy, Iii. The spreading of fluids on glass, Lond. Edinb. Dublin Philos. Mag. J. Sci. 38 (223) (1919) 49–55.

[24] Cyril W. Hirt, Billy D. Nichols, Volume of fluid (vof) method for the dynamics of free boundaries, J. Comput. Phys. 39 (1) (1981) 201–225.

[25] David B. Hough, Lee R. White, The calculation of hamaker constants from liftshitz theory with applications to wetting phenomena, Adv. Colloid Interface Sci. 14 (1) (1980) 3–41.

[26] Chun Huh, L.E. Scriven, Hydrodynamic model of steady movement of a solid/liquid/fluid contact line, J. Colloid Interface Sci. (ISSN 0021-9797) 35 (1) (1971) 85–101, https://doi.org/10.1016/0021-9797(71)90188-3, https://www.sciencedirect.com/science/article/pii/0021979771901883.

[27] Jacob N. Israelachvili, Intermolecular and Surface Forces, Academic Press, 2011.

[28] Mohammad Jafari, Jongwon Jung, Variation of contact angles in brine/co2/mica system considering short-term geological co2 sequestration condition, Geofluids (2018) 2018, https://doi.org/10.1155/2018/3501459.

[29] Jong-Won Jung, Jiamin Wan, Supercritical co2 and ionic strength effects on wettability of silica surfaces: equilibrium contact angle measurements, Energy Fuels 26 (9) (2012) 6053–6059.

[30] I. Kuchin, Victor Starov, Hysteresis of contact angle of sessile droplets on smooth homogeneous solid substrates via disjoining/conjoining pressure, Langmuir 31 (19) (2015) 5345–5352.

[31] Hassan Mahani, Arsene Levy Keya, Steffen Berg, Willem-Bart Bartels, Ramez Nasralla, William R. Rossen, Insights into the mechanism of wettability alteration by low-salinity flooding (lsf) in carbonates, Energy Fuels 29 (3) (2015) 1352–1367.

[32] Mahdi Mansouri-Boroujeni, Cyprien Soulaine, Mohamed Azaroual, Sophie Roman, How interfacial dynamics controls drainage pore-invasion patterns in porous media, Adv. Water Resour. (ISSN 0309-1708) 171 (2023) 104353, https://doi.org/10.1016/j.advwatres.2022.104353, https://www.sciencedirect.com/science/article/pii/S0309170822002160.

[33] Vladimir S. Mitlin, Dewetting of solid surface: analogy with spinodal decomposition, J. Colloid Interface Sci. (ISSN 0021-9797) 156 (2) (1993) 491–497, https://doi.org/10.1006/jcis.1993.1142, https://www.sciencedirect.com/science/article/pii/S0021979783711422.

[34] Ian L. Molnar, Denis M. O'carroll, Jason I. Gerhard, Impact of surfactant-induced wettability alterations on dnapl invasion in quartz and iron oxide-coated sand systems, J. Contam. Hydrol. 119 (1–4) (2011) 1–12.

[35] Alexander Oron, Stephen H. Davis, S. George Bankoff, Long-scale evolution of thin liquid films, Rev. Mod. Phys. 69 (3) (1997) 931.

[36] A. Pourakaberian, H. Mahani, V. Niasar, The impact of the electrical behavior of oil-brine-rock interfaces on the ionic transport rate in a thin film, hydrodynamic pressure, and low salinity waterflooding effect, Colloids Surf. A, Physicochem. Eng. Asp. 620 (2021) 126543.

[37] Osborne Reynolds, Iv. on the theory of lubrication and its application to mr. beauchamp tower's experiments, including an experimental determination of the viscosity of olive oil, Philos. Trans. R. Soc. Lond. 177 (177) (1886) 157–234.

[38] Sophie Roman, Cyprien Soulaine, Anthony R. Kovscek, Pore-scale visualization and characterization of viscous dissipation in porous media, J. Colloid Interface Sci. (ISSN 0021-9797) 558 (2020) 269–279, https://doi.org/10.1016/j.jcis.2019.09.072, http://www.sciencedirect.com/science/article/pii/S0021979719311166.

[39] Anthony M. Schwartz, Charles A. Rader, Elaine Huey, Resistance to flow in capillary systems of positive contact angle, 1964.

[40] Pierre Seppecher, Moving contact lines in the Cahn-Hilliard theory, Int. J. Eng. Sci. 34 (9) (1996) 977–992.

[41] J.J. Sheng, Critical review of low-salinity waterflooding, J. Pet. Sci. Eng. (ISSN 0920-4105) 120 (2014) 216–224, https://doi.org/10.1016/j.petrol.2014.05.026, http://www.sciencedirect.com/science/article/pii/S0920410514001430.

[42] Yulii D. Shikhmurzaev, Capillary Flows with Forming Interfaces, CRC Press, 2007.

[43] Nikolai Siemons, Hans Bruining, Hein Castelijns, Karl-Heinz Wolf, Pressure dependence of the contact angle in a co2–h2o–coal system, J. Colloid Interface Sci. (ISSN 0021-9797) 297 (2) (2006) 755–761, https://doi.org/10.1016/j.jcis.2005.11.047, http://www.sciencedirect.com/science/article/pii/S0021979705012245.

[44] Š Šikalo, H-D. Wilhelm, I.V. Roisman, S. Jakirlić, C. Tropea, Dynamic contact angle of spreading droplets: experiments and simulations, Phys. Fluids 17 (6) (2005) 062103.

[45] Juan Song, Dongxiao Zhang, Comprehensive review of caprock-sealing mechanisms for geologic carbon sequestration, Environ. Sci. Technol. 47 (1) (2013) 9–22, https://doi.org/10.1021/es301610p.

[46] Cyprien Soulaine, Julien Maes, Sophie Roman, Computational microfluidics for geosciences, Front. Water 3 (2021) 1–11, https://doi.org/10.3389/frwa.2021.643714.

[47] Dag C. Standnes, Tor Austad, Wettability alteration in chalk: 2. mechanism for wettability alteration from oil-wet to water-wet using surfactants, J. Pet. Sci. Eng. (ISSN 0920-4105) 28 (3) (2000) 123–143, https://doi.org/10.1016/S0920-4105(00)00084-X, http://www.sciencedirect.com/science/article/pii/S092041050000084X.

[48] Mirhossein Taheriotaghsara, Maria Bonto, Hamid M. Nick, Ali Akbar Eftekhari, Estimation of calcite wettability using surface forces, J. Ind. Eng. Chem. 98 (2021) 444–457.

[49] Guo-Qing Tang, Abbas Firoozabadi, Wettability alteration to intermediate gas-wetting in porous media at elevated temperatures, Transp. Porous Media 52 (2) (2003) 185–211.

[50] L.H. Tanner, The spreading of silicone oil drops on horizontal surfaces, J. Phys. D, Appl. Phys. 12 (9) (1979) 1473.

[51] Gary F. Teletzke, H. Ted Davis, L.E. Scriven, How liquids spread on solids, Chem. Eng. Commun. 55 (1–6) (1987) 41–82.

[52] Ichiro Ueno, Kanji Hirose, Yusuke Kizaki, Yoshiaki Kisara, Yoshizumi Fukuhara, Precursor film formation process ahead macroscopic contact line of spreading droplet on smooth substrate, J. Heat Transf. 134 (5) (2012).

[53] E.J. Verwey, J. Th, G. Overbeek, K. van Nes, Theory of the Stability of Lyophobic Colloids: the Interaction of Sol Particles Having an Electric Double Layer, Elsevier Pub. Co., 1948.

[54] O.V. Voinov, Hydrodynamics of wetting, Fluid Dyn. 11 (5) (1976) 714–721.

[55] Dan Wang, Gang Peng, Yajun Yin, The van der Waals potential between arbitrary micro/nano curved surfaces in curvature-based form, Chem. Phys. Lett. (ISSN 0009-2614) 759 (2020) 137907, https://doi.org/10.1016/j.cplett.2020.137907, https://www.sciencedirect.com/science/article/pii/S0009261420308228.

[56] Stephen K. Wilson, Hannah-May D'Ambrosio, Evaporation of sessile droplets, Annu. Rev. Fluid Mech. 55 (2023) 481–509.

[57] Alexander W. Wray, Demetrios T. Papageorgiou, Richard V. Craster, Khellil Sefiane, Omar K. Matar, Electrostatic suppression of the "coffee stain effect", Langmuir 30 (20) (2014) 5849–5858.

[58] Qingfang Wu, Harris Wong, A slope-dependent disjoining pressure for non-zero contact angles, J. Fluid Mech. 506 (2004) 157–185.

[59] Daoyong Yang, Paitoon Tontiwachwuthikul, Yongan Gu, Interfacial interactions between reservoir brine and co2 at high pressures and elevated temperatures, Energy Fuels 19 (1) (2005) 216–223, https://doi.org/10.1021/ef049792z.

[60] E.K. Yeh, John Newman, C.J. Radke, Equilibrium configurations of liquid droplets on solid surfaces under the influence of thin-film forces: part I. Thermodynamics, Colloids Surf. A, Physicochem. Eng. Asp. (ISSN 0927-7757) 156 (1) (1999) 137–144, https://doi.org/10.1016/S0927-7757(99)00065-5, https://www.sciencedirect.com/science/article/pii/S0927775799000655.

[61] Benzhong Zhao, Christopher W. MacMinn, Ruben Juanes, Wettability control on multiphase flow in patterned microfluidics, Proc. Natl. Acad. Sci. 113 (37) (2016) 10251–10256, https://doi.org/10.1073/pnas.1603387113, http://www.pnas.org/content/113/37/10251.abstract.

[62] Liya Zhornitskaya, Andrea L. Bertozzi, Positivity-preserving numerical schemes for lubrication-type equations, SIAM J. Numer. Anal. 37 (2) (1999) 523–555.